# Earthquakes analysis using data recorded by the Stanford DAS Array

*Biondo Biondi, Eileen Martin, Steve Cole, and Martin Karrenbach*

## ABSTRACT

We analyze the data recorded by the "Stanford DAS Array" for 6 seismic events cataloged in the USGS online database. Two of these events are man made (blasts at a nearby quarry), and 4 are earthquakes spanning a range from a local event that occurred less than 4 km from the array to a large quake offshore Cape Mendocino in North California. The data from two seismometers installed on Stanford campus at Jasper Ridge help to validate and interpret the data recorded by our DAS array. The analysis of the two quarry-blasts demonstrates that both kinematics and waveforms are recorded by the DAS array with excellent repeatability. We show that the time of the first-break of P-wave arrivals can be reliably measured from the DAS array, notwithstanding the loose coupling of the fiber-optic cable with the ground, and the known limitations of DAS to record events with particle motion orthogonal to the fiber cable. P-wave waveforms are more challenging to analyze because of the complexity of the wavefield, probably caused by strong local scattering. All the events we analyzed show that kinematics of S and surface waves can be reliably measured from the data recorded by our DAS array. Because of noise and uncertain coupling, it is more challenging to assess the quality of the waveform shapes and amplitudes than the kinematics. We show that that DAS recording of propagating waves with particle displacement orthogonal to the propagation direction are subject to a phase rotation that is dependent on the fiber-cable direction. When we apply an approximate correction for this phase rotation the spatial coherency of S-wave and surface-wave arrivals substantially improves.

## INTRODUCTION

One of the main goals of our "Stanford DAS Array-1" (SDASA-1) experiment (Martin et al., 2017b,a) is to evaluate the feasibility of using fiber-optics as Distributed Acoustic Sensors (DAS) to detect and analyze earthquake data. DAS arrays have the potential of enabling cost-effective continuous and spatially dense seismic monitoring over large areas. This application of DAS technology has implications for managing earthquake hazard in densely populated areas at high seismic risk (e.g. the San Francisco Bay Area) as well as for reservoir management when seismic events are caused by either injection or extraction of fluids. Our experiment is unique because

we are recording data from a fiber-optic cable laying in a PVC conduit buried in the ground. Coupling between the fiber cable and the surrounding rocks relies exclusively on gravity and friction. This recording configuration could deliver huge savings by enabling the exploitation of existing infrastructure developed for telecommunication purposes (like in our experiment) or the use of ad-hoc inexpensive "slim-holes" with PVC casing buried sufficiently deep to bypass the near-surface and avoid its negative effects on the recorded data.

Because SDASA-1 has been continuously recording data starting in September 2016 and California is tectonically active, we have a large number of events to analyze. We focus on four naturally-occurring events that span the full range from weak and nearby earthquakes to strong and far away ones. In our analysis we also included two blasts from a nearby quarry that are ideal to test the repeatability of the recording. To validate the events observed in SDASA-1 data, we use the USGS earthquake online database and the data recorded at the "Jasper Ridge Biological Preserve" (JRSC station) by two seismometers that are managed by the Berkeley Digital Seismic Network. Data from JRSC are available online. The Jasper Ridge station is located about 6.4 km from the SDASA-1. Because near-surface conditions are different below SDASA-1 and JRSC the waveforms are not directly comparable. However, JRSC data provide a rough indication of the arrival time and relative strength of the signal corresponding to different arrivals (e.g. P-waves, S-waves, and surface waves).

In the next section we provide a brief description of the experimental setup and of the events that we used in our study. We then analyze the recordings by the SDASA-1 in details, and compare them with the corresponding data recorded at Jasper Ridge.

## EXPERIMENT SETUP

Martin et al. (2017a) provide most of the relevant information on the SDASA-1 experiment. Here we provide additional information on the experiment setup that is important for interpreting the results discussed in the following section.

Figure 1 shows the layout of the array; its double-loop path is outlined by the red line. The annotations indicate the channel numbers at the array corner points. The channel numbering starts at #5, outside of the Green Earth Sciences Building where the laser interrogator is installed, and increases as we move westward along the path.

As mathematically demonstrated in Appendix A, elastic waves are recorded by the DAS array with a scaling and phase rotation dependent on the angle between the propagation direction and the fiber direction. In particular, waves with particle displacement normal to the propagation direction are recorded with opposite polarity by two segments of SDASA-1 oriented in orthogonal directions (N-S vs. E-W). To make the spatial continuity of some of the arrivals more apparent, when plotting some of the figures we have scaled the amplitudes of each channel by either -1 or +1, depending on whether the fiber cable was directed in the N-S direction (+1) or

E-W direction (-1). Figure 2 displays this scaling factor as a function of the channel number.

## Jasper Ridge seismic station (JRSC)

JRSC was installed in 1994 by a team from Stanford Geophysics (Robert Kovach and Greg Beroza), the USGS, and UC Berkeley. It is part of a network of seismic stations in northern and central California maintained and operated by the Berkeley Digital Seismic Network (BDSN). The station consists of two 3-components seismometers. A broad-band seismometer (JRSC-BB): Streckeisen STS-2 VBB Tri-Axial Seismometer, and a long-period accelerometer (JRSC-LP): TSA-100S (4 g max 5 v/g). Data are available for downloading sampled at 0.025 s for JRSC-BB and at 1 s for JRSC-LP. The seismometers sit on a concrete pad inside a preexisting cave on the west shore of Searsville Lake. The cave is located 36 m above sea level and 6.4 km to the SWW of SDASA-1.

## Seismic events

In the following section we analyze seismic data recorded by the SDASA-1 and compare them with data recorded by JRSC. Since we activated the array in September 2016 we recorded many seismic events. Our analysis is limited to 6 events that are representative of the whole range of events recorded by the array. The following list provide the main characteristics of these 6 events in order of increasing magnitude:

- *Blast #1*: September 14, 2016 – M 1.3 – z=-0.3 km – $\Delta$=14.40 km to SSE,
- *Blast #2*: November 4, 2016 – M 1.6 – z=-0.3 km – $\Delta$=14.05 km to SSE,
- *Ladera*: January 11, 2017 – M 2.0 – z=4.2 km – $\Delta$=3.86 km to SW,
- *Bonny Doon*: October 27, 2016 – M 2.5 – z=13.1 km – $\Delta$=37.80 km to SSW,
- *Piedmont*: September 12, 2016 – M 3.5 – z=4.0 km – $\Delta$=42.00 km to N,
- *Ferndale*: September 2, 2016 – M 5.6 – z=28.6 km – $\Delta$=443 km to NW.

The magnitude (M) and depth (z) of each event are based on the online USGS database. The distance from SDASA-1 ($\Delta$) is estimated using Google map. The date is in local California time. In the following we will refer to each individual event by the corresponding label typeset in italic, as in the list above (e.g. *Blast #1.*)

The first two events are artificial blasts at a nearby quarry; their source locations are separated by only 350 meters, and thus their source waveforms and propagation paths are presumably similar. These two events are useful to evaluate the repeatability of the recording. The other 4 events are naturally occurring earthquakes, ranging

from local and fairly shallow ones, to much stronger and deeper quakes. The USGS website provides further information on the source mechanism of events with magnitude equal or larger than 2. We are not reporting this information since our analysis is not using it, but more detailed analysis could correlate the observed waveforms to the estimated source mechanisms.

# DATA ANALYSIS

We present the analysis of the data recorded by SDASA-1 and JRSC for the 6 events listed above by focusing on one important issue at the time: 1) signal repeatability, 2) P-wave arrivals, and 3) S-wave and surface-wave arrivals.

## Signal repeatability

Because of the weak signals and strong environmental noise, in particular during the day, the first-order question that our analysis aimed to answer is whether the events that we observe in the recorded data correspond to actual seismic events. Fortunately, the vicinity with a quarry provided us with several recordings of artificial blasts that can be used to assess the repeatability of the observed arrivals. This analysis leads to the conclusions that indeed the recorded events are repeatable and directly correlated to quarry blasts.

The top panel in Figure 3 shows the data recorded by SDASA-1 after noise attenuation and bandpassing from 0.25 to 2.5 Hz. The DAS channels were scaled by the scaling function shown in Figure 2 before plotting. The origin of the time axis is the time of *Blast #1* as provided by the USGS online database. We use the same convention to set the origin of the time axis for all the data displays that follow. The trace at the bottom shows the data recorded by the North component of JRSC-BB. This trace was bandpassed with the same filter as the DAS data; that is, from 0.25 to 2.5 Hz. All the data displays that follow show JRSC data bandpassed using the same parameters used to bandpass the corresponding DAS data. The channel numbers in all the figures correspond to the channels numbers marked on the map in Figure 1. The strong slowly-propagating events visible around channel #150 were generated by vehicles passing close to the array. This vehicle-related noise is visible in most of the recording, with the exception of the data corresponding to the *Piedmont* event that occurred just before midnight.

Figure 4 shows the data recorded by SDASA-1 corresponding to *Blast #2* and the corresponding North component recorded by JRSC-BB. *Blast #2* occurred less than two month after *Blast #1* and had a higher magnitude (1.6 vs. 1.3); the source location was about 350 m to the North of *Blast #1* source location. The timing and waveform are consistent between these two events, with a slight time shift caused by the shift in source location. Because of the time delays from the blasts, we interpreted these events as surface waves generated by the blasts and being recorded by SDASA-1.

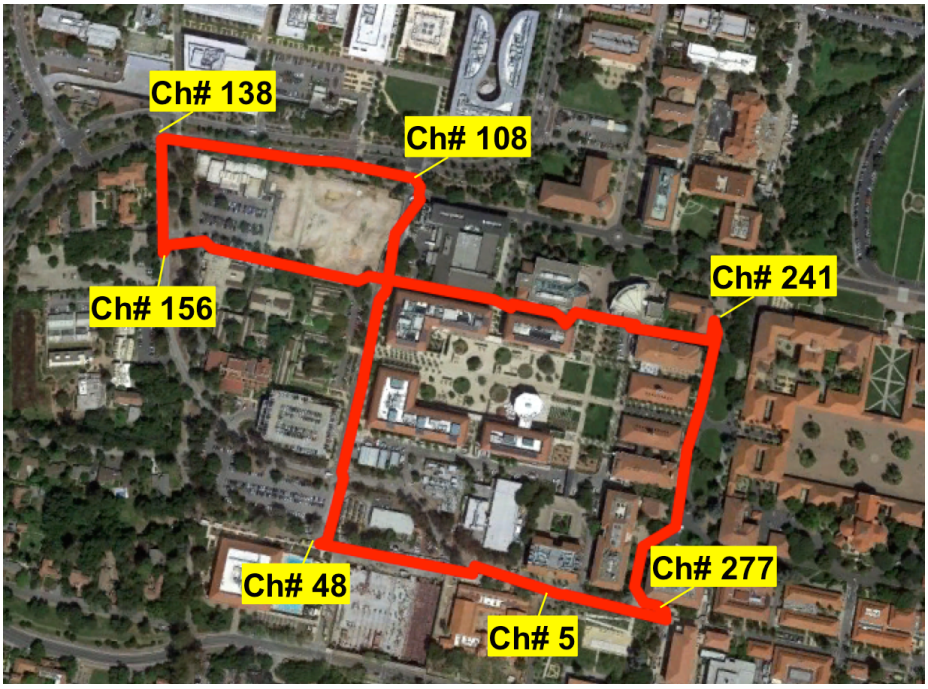


Figure 1: Map showing the path of SDASA-1 with the location of the corner points of the array marked and labeled with the corresponding channel numbers. [**NR**]

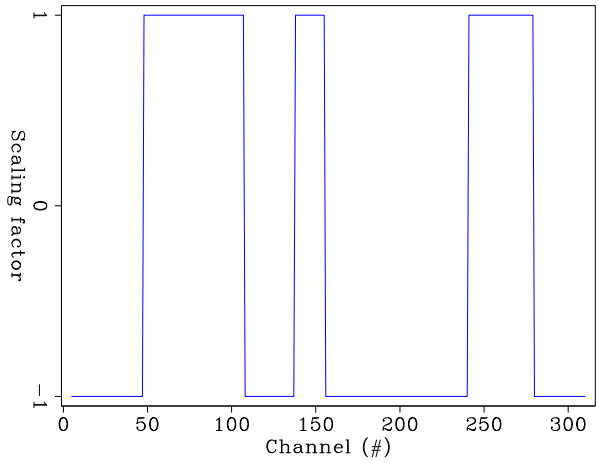


Figure 2: Scaling factor used for some of the data displays. Channels where the fiber cable is oriented in the N-S direction are weighted by +1, whereas the ones where the fiber cable is oriented in the E-W direction are weighted by -1. [**ER**]

In both *Blast #1* and *Blast #2* recordings, the time shifts of the events across the array match the relative distances from the sources of the recording channels; the events arrive at the southern side of the array (edges) almost 0.5 s before they arrive at its Northern side (middle) (see Figure 1.)

At least for these quarry blasts, it is easier and more reliable to detect the events from the SDASA-1 data than from the data recorded by the seismometers at Jasper Ridge. It would be impossible to detect the blasts from any of the traces recorded by JRSC (all three components of JRSC-BB and JRSC-LP.) In these recordings the signal does not rise above the noise level, as exemplified by the North components displayed at the bottom of Figures 3 and 4.

## P-wave kinematics and waveforms

Next issue that we address is whether we can extract reliable kinematic information about P-wave arrivals from data recorded by SDASA-1. Figures 5 and 6 demonstrate that the timing of the P-wave arrivals can be easily picked from the SDASA-1 data.

The top panel in Figure 5 shows the envelope of the data recorded by SDASA-1 corresponding to the *Piedmont* event. The envelope was computed after noise attenuation and high-passing above 0.25 Hz. The trace at the bottom shows the data recorded by the vertical component of JRSC-BB. The amplitude jump in the envelope function is easily identifiable and the arrival time is consistent with the arrival time at JRSC-BB. There is a time shift of approximately .25 s between SDASA-1 and JRSC data that is due to the relative distance from the source location. Piedmont is almost perfectly North of Stanford and JRSC is approximately 2.5 km South of SDASA-1. The time-shifts within the array are also consistent with an event arriving from the North. They are much smaller than the time shifts of the surface waves observed in Figures 3 and 4 because P-waves generated at this distance (42 km) emerge at the surface at a fairly steep angle.

The top panel in Figure 6 shows the envelope of the data recorded by SDASA-1 corresponding to the *Ladera* event. In this case the event is much closer to JRSC than to SDASA-1, and thus the time of the first break at JRSC-BB (bottom trace) is about a third of the first-break time at SDASA-1. As in the *Piedmont* case, the relative arrival times across the array are consistent with a S-W direction of the source. However, the picking of first breaks would be more challenging in this case than in the previous one because of environmental noise. The first channels to record the event are around the SW corners of the array; that is, around Channel #48 and around Channel #156.

The vertical component recorded at JRSC-BB (bottom panel in Figure 6) shows clearly the arrival of the P-waves, the S-waves, and of the surface waves. The sudden increase in amplitudes of the envelope function at about 3.8 s is most probably caused by the arrival of the S-waves at SDASA-1. Unfortunately, because of the proximity of the *Ladera* event, the JRSC-BB data cannot be used to estimate the timing of the

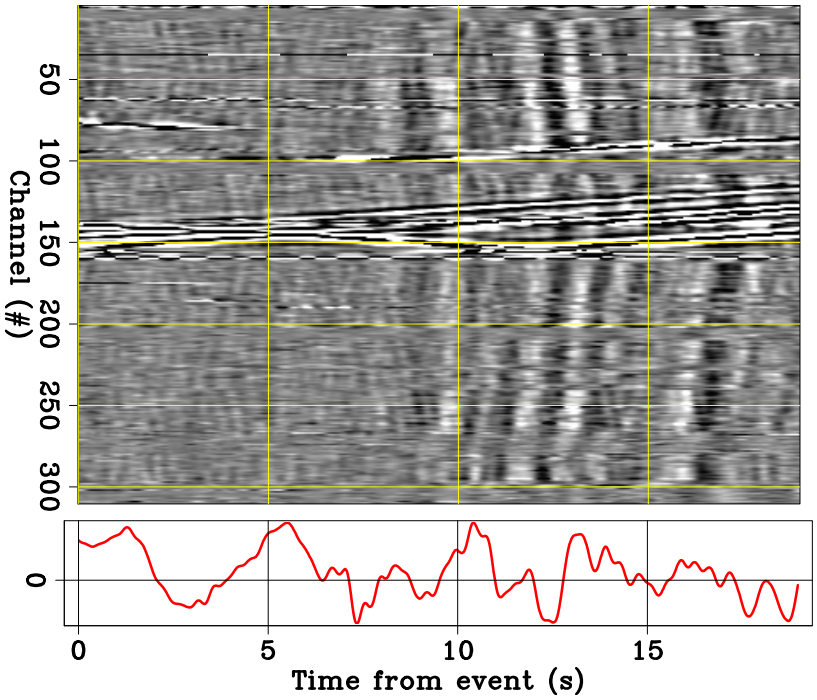


Figure 3: Data recorded for the *Blast #1* event after bandpassing (0.25–2.5 Hz) and channel-dependent scaling by the function shown in Figure2. Top: SDASA-1 array; bottom: JRSC-BB North component. [**ER**]

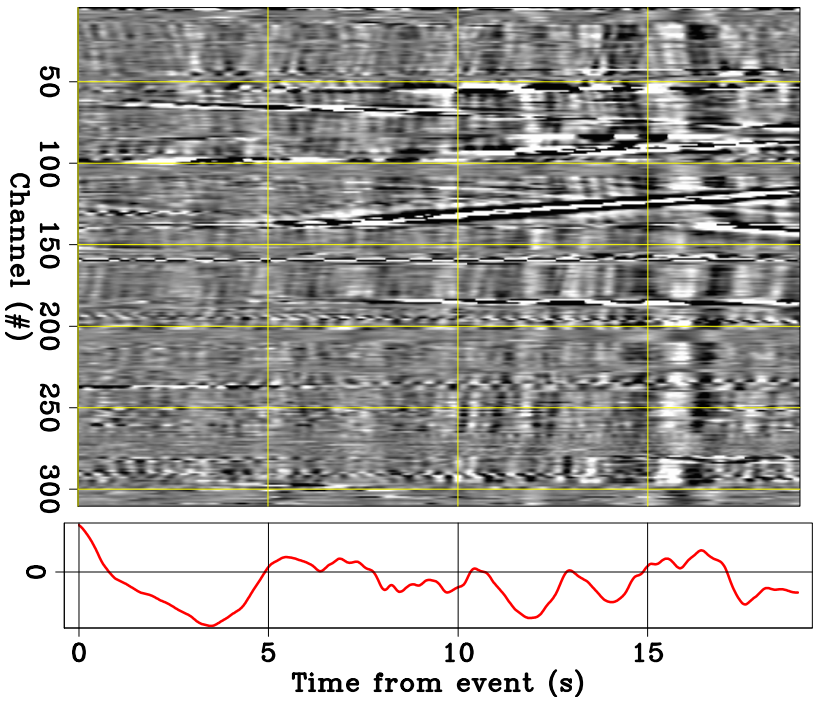


Figure 4: Data recorded for the *Blast #2* event after bandpassing (0.25–2.5 Hz) and channel-dependent scaling by the function shown in Figure2. Top: SDASA-1 array; bottom: JRSC-BB North component. [**ER**]

S-wave arrival at SDASA-1, and thus to validate this interpretation.

In contrast with the kinematics of the P-wave arrivals that are clearly measurable from the SDASA-1 data, the waveforms are not as well preserved. Figures 7 and 8 show the data from which the envelope functions shown in Figures 5 and 6 were computed. In Figure 8 we can identify several coherent arrivals between 2.5 s and 3.5 s that are related to the first P-wave arrival and to complex scattering along the wavepaths. The recorded wavefield is complex because of scattering, but the recording is also suffering from the effect of imperfect coupling and of the known strong directional sensitivity of the DAS sensor (Kuvshinov, 2016).

## S-wave and surface-wave kinematics and waveforms

Figure 6 shows an example where the kinematic of S-waves can be estimated from the SDASA-1 data. However, it is more difficult to identify S-arrivals than surface-wave arrivals, not only from SDASA-1 data, but also from JRSC data. Figures 9 and 10 show an example of this challenge. The top panel in Figure 9 shows the data recorded for the *Bonny Doon* event after noise reduction and bandpassing from .25 to 1.0 Hz. The trace at the bottom shows the corresponding North component of JRSC-BB. Figure 10 shows the same data as in Figure 9, but after applying the scaling function shown in Figure 2 to the SDASA-1 data. The polarity flipping performed by the scaling helps the identification of S-waves and surface-waves as coherent arrivals across the array.

Surface waves arriving at about 16 s are clearly identifiable in both SDASA-1 and JRSC data. In the SDASA-1 data, the time differences between channels of these arrivals are similar to the ones observed from the quarry blasts (Figures 3 and 4.) There are a few notable differences related to the slight difference in arrival direction. The blasts arrived from the SEE direction, whereas the *Bonny Doon* event arrived from the SWW direction. The most obvious difference is that the *Bonny Doon* arrival has no moveout along the longest leg of the array (Channel #156 to Channel #241) because it arrives along a direction almost perfectly orthogonal to the fiber-cable direction. On the contrary, the blasts events have a slight, but clearly observable, negative moveout along this same leg; the blasts arrive before at the eastern channels than at the western ones.

Both the SDASA-1 data and the JRSC data show some possible arrivals at around 5 s and 11 s. They could be interpreted the P-wave and S-wave arrivals, respectively. A large uncertainty would be associated with this interpretation. This uncertainty would be greatly reduced if we had data from a wider DAS array since we would be able to measure moveouts more reliably across a wider array than across SDASA-1. These moveouts are not measurable from our fairly narrow array because body-waves emerge at the surface almost vertically.

The last event we examine is *Ferndale*. This is a large (M=5.6) and deep event originated along the Mendocino Fault under the Pacific Ocean more than 400 km to

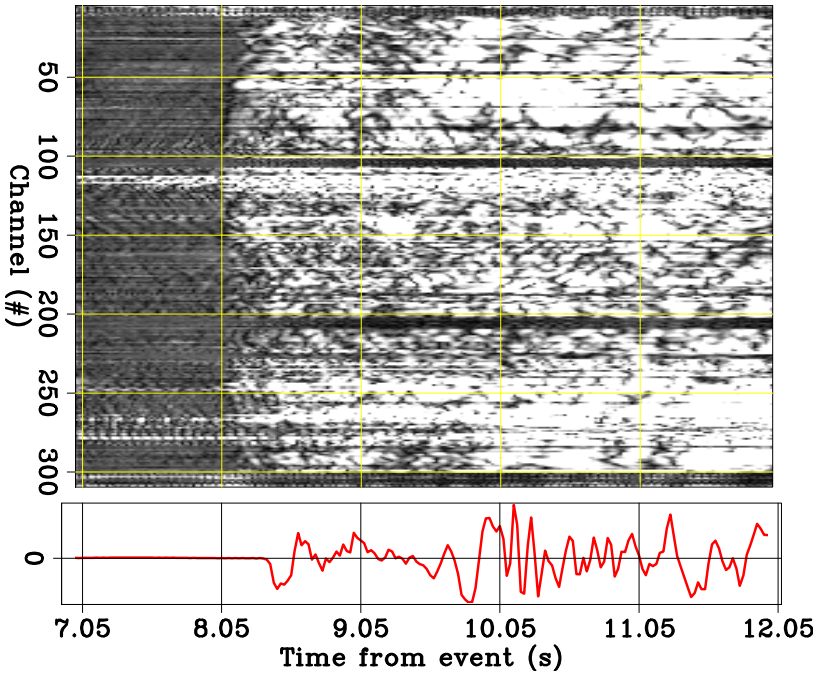


Figure 5: Data recorded for the *Piedmont* event after high-passing ($\geq 0.25$ Hz). Top: Envelope of SDASA-1 array data; bottom: JRSC-BB vertical component. [**ER**]

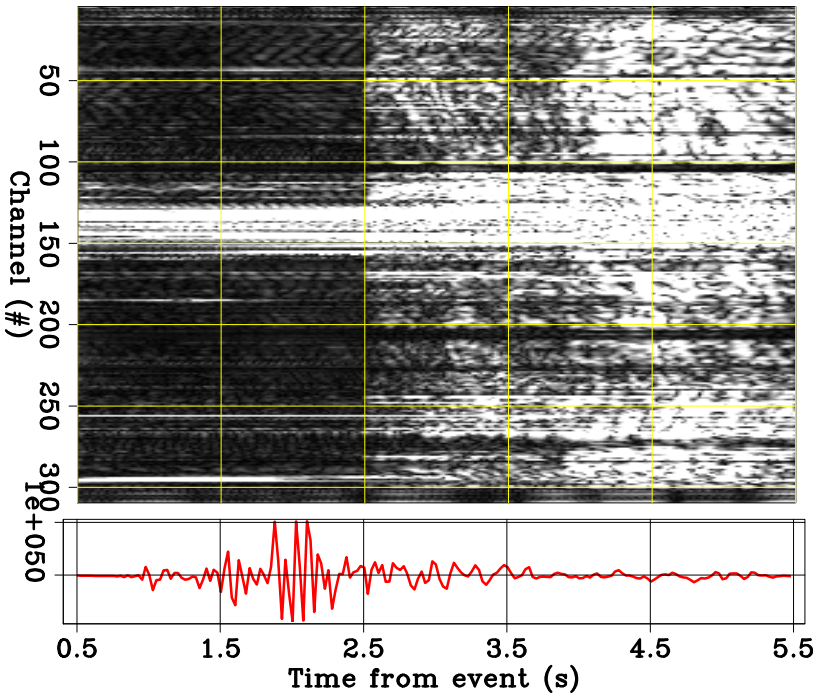


Figure 6: Data recorded for the *Ladera* event after high-passing ($\geq 0.25$ Hz). Top: Envelope of SDASA-1 array data; bottom: JRSC-BB vertical component. [**ER**]

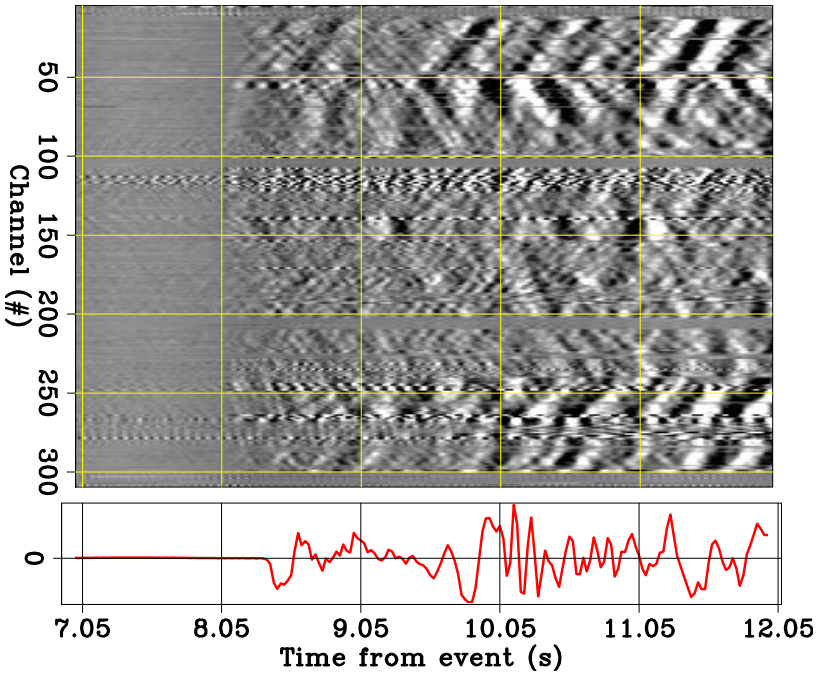


Figure 7: Data recorded for the *Piedmont* event after high-passing ($\geq 0.25$ Hz). Top: SDASA-1 array; bottom: JRSC-BB vertical component. [**ER**]

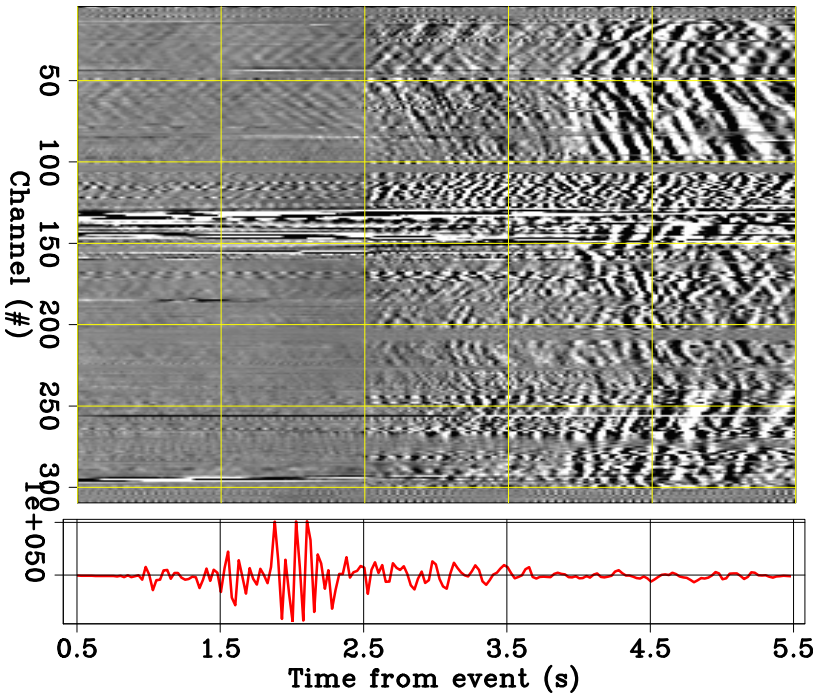


Figure 8: Data recorded for the *Ladera* event after high-passing ($\geq 0.25$ Hz). Top: SDASA-1 array; bottom: JRSC-BB vertical component. [**ER**]

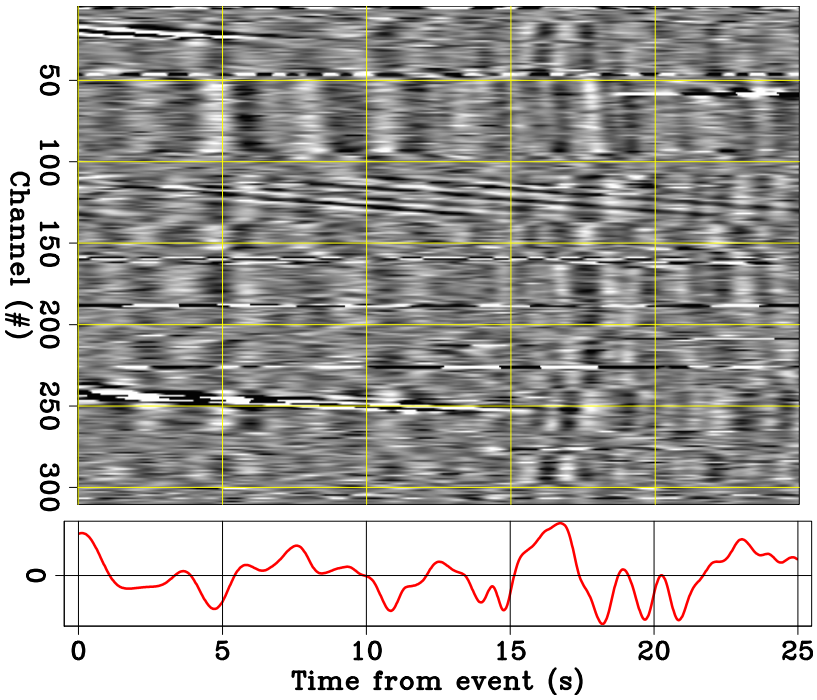


Figure 9: Data recorded for the *Bonny Doon* event after bandpassing (0.25–1.0 Hz). Top: SDASA-1 array; bottom: JRSC-BB North component. [**ER**]

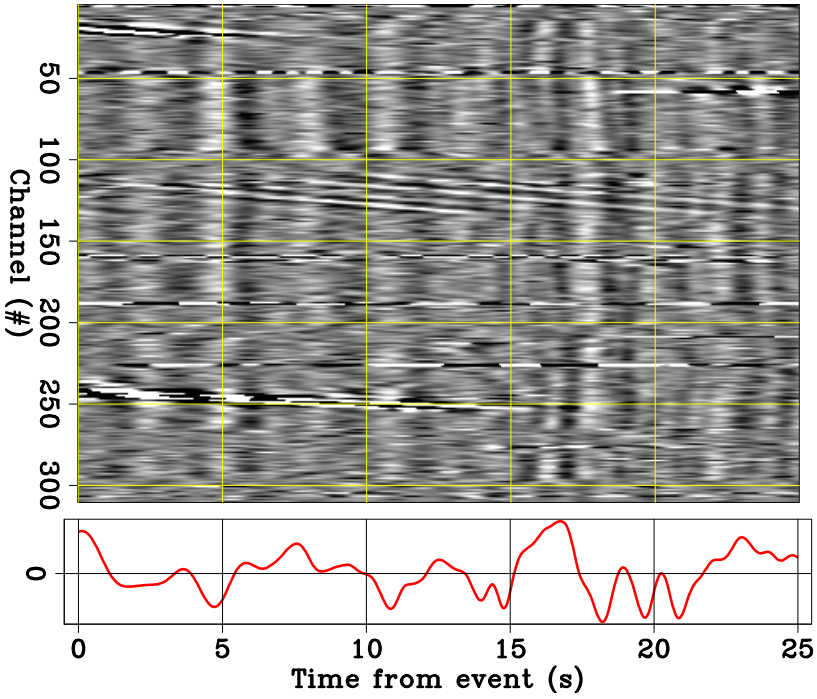


Figure 10: Data recorded for the *Bonny Doon* event after bandpassing (0.25–1.0 Hz) and channel-dependent scaling. Top: SDASA-1 array; bottom: JRSC-BB North component. [**ER**]

the NW of Stanford. For this event we observe strong S-wave and surface-wave arrivals at both SDASA-1 and JRSC. Figure 11 shows the S-wave arrivals. The trace at the bottom shows the North component of JRSC-BB. The data were bandpassed from .25 to 1 Hz, and the data from the SDASA-1 were scaled before displaying. Fortunately, during the *Ferndale* event the vehicle noise was not as strong as during other events. Therefore, we could preserve the original data dynamic range when plotting the SDASA-1 data; that is, we clipped only the highest amplitudes (pclip=99.5). In both recordings, the S-arrival rises above the noise after a fairly quite period and it easily detectable.

The relative timing of the arrivals across the array is more challenging to interpret than for previous events. The arrival time has a local minimum close to the NW corner of the array (Channel #138). However away from that zone, the arrivals have more complex and not as easily interpretable moveouts. Given the long path from source to receivers, these behavior may be explained by ray bending, as well as by near-surface heterogeneities close to SDASA-1.

Finally, Figure 12 shows the data window around the surface-wave arrivals. As for the previous figure, we plotted the SDASA-1 data preserving the data dynamic range. Both SDASA-1 and JRSC data show clearly the first surface-waves arriving after a quite period. Similarly to the analysis of S-wave arrivals above, the kinematics across the array are more difficult to interpret but the arrival time has a local minimum close to the NW corner of the array (Channel #138).

## CONCLUSIONS AND FUTURE WORK

The analysis of six seismic events recorded by SDASA-1 demonstrate the suitability of this kind of arrays for cost-effective recording of seismic events. We showed that a wealth of useful information can be extracted from the recorded data, notwithstanding the expected limitations in the fidelity of the recording caused by the strong directional sensitivity of DAS sensors, and imperfect coupling between the fiber cable and the ground in our open-conduit installation.

We have shown that reliable kinematic information is well preserved in the recorded data for all arrivals (P-waves, S-waves and surface waves.) A more detailed and quantitative analysis should be performed on the reliability of the information that can be extracted from the data on waveform shapes and amplitudes. We plan to install 2-3 broad-band seismometers in the manholes where the fiber cable is currently installed. These seismometers should provide invaluable reference data to perform a more quantitative analysis on the data collected by SDASA-1. Furthermore, as the array is continuously operating, we are accumulating a large database of many events of all magnitudes, coming from all directions, and with a broad range of source mechanisms. If appropriately mined, possibly by using novel data-analytic algorithms, this database will enable much more detailed analysis.

The comparison of the data recorded using our current laser interrogator with

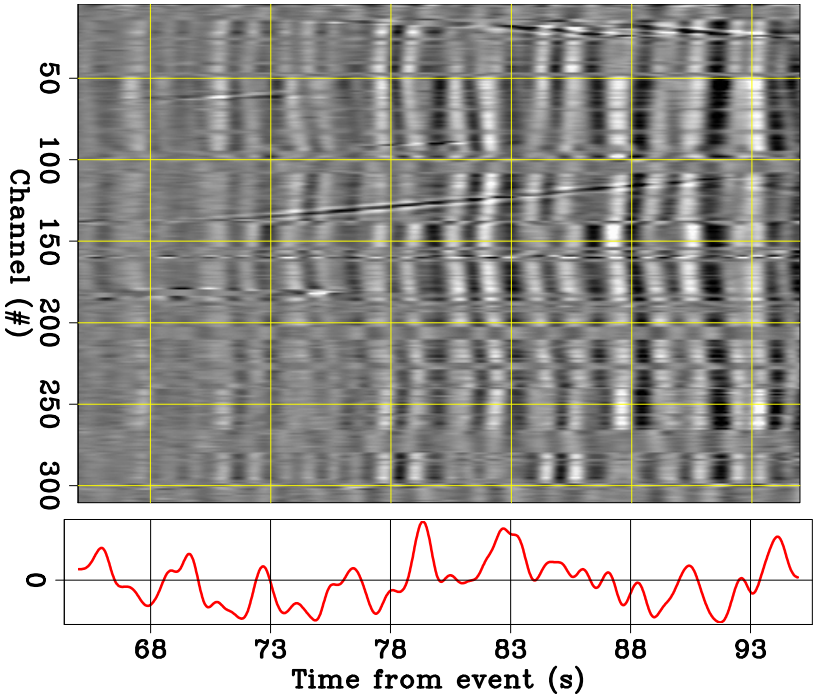


Figure 11: Data recorded for the *Ferndale* event after bandpassing (0.25–1.0 Hz) and channel-dependent scaling. Top: SDASA-1 array; bottom: JRSC-BB North component. [**ER**]

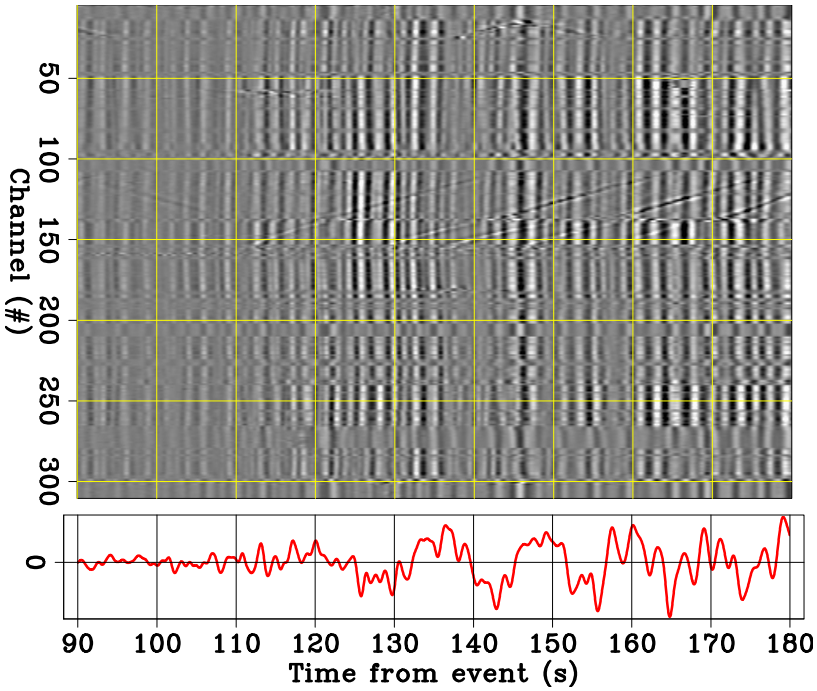


Figure 12: Data recorded for the *Ferndale* event after bandpassing (0.25–1.0 Hz) and channel-dependent scaling. Top: SDASA-1 array; bottom: JRSC-BB North component. [**ER**]

the data recorded using a latest-generation interrogator would also provide extremely useful information. In particular, we could leverage the repeatability of the quarry blasts to quantitatively analyze differences in data quality observed with different laser interrogators. This analysis could lead to quantitative evaluation of the limits on the data quality imposed by the coupling of the fiber cable (that we do not expect to improve in similar open-conduit installations) versus the limitations of the laser interrogators, that we expect to substantially improve as the technology progress.

Finally, data recorded from a broader array that could be easily deployed using Stanford's extensive fiber infrastructure would provide extremely useful information. As discussed in the paper, for body-wave arrivals the moveouts across the array are small, and thus do not enable the use of beamforming or other "array processing" methods. However, the reliability of the kinematic information that we measure from SDASA-1 suggests that a wider array (SDASA-2?) would enable much more detailed analysis of seismic events originating around, or below, the Bay Area.

## ACKNOWLEDGMENTS

We would like thank OptaSense Ltd for making the DAS recording equipment available and supporting the work of two of the authors. We would like also to thank Gregory Kersey, Paul Narcisse, and Gary Gutfeld with the Fiber Team within Stanford IT Services for their support and patience.

## REFERENCES

Kuvshinov, B., 2016, Interaction of helically wound fibre-optic cables with plane seismic waves: Geophysical Prospecting, **64**, 671–688.

Martin, E., B. Biondi, S. Cole, and M. Karrenbach, 2017a, Overview of the Stanford DAS Array-1 (SDASA-1) : SEP-Report, **168**, 1–10.

Martin, E., B. Biondi, M. Karrenbach, and S. Cole, 2017b, Continuous Subsurface Monitoring by Passive Seismic with Distributed Acoustic Sensors: the "Stanford Array" experiment: Presented at the "First EAGE Workshop on "Practical Reservoir Monitoring", Eur. Assoc. Expl. Geophys.

## APPENDIX A

In this appendix we develop the theory showing that elastic waves impinging on a DAS array are recorded with different amplitude scaling and phase rotation depending on whether the particle displacement is aligned with the propagation direction (e.g. P-waves) or orthogonal to it (e.g. S-waves and Love waves).

We present the case for 2D propagation. We have not fully developed the 3D case yet. However, it is probably required to understand the phase-rotation of Rayleigh

waves recorded by SDASA-1.

## 2D propagation in the same direction as particle motion

The analysis that follows is relevant to P-waves and the horizontal component of Rayleigh waves. We'll use a coordinate system $(r_1, r_2)$ where $r_1$ is the propagation direction as well as the particle displacement direction. The expression for displacement at position $(r_1, r_2)$ and time $t$ of a monochromatic plane wave with frequency $\omega$ and wavenumber $k$ is

$$\mathbf{d}(r_1, r_2, t) = (\cos(kr_1 - \omega t), 0), \tag{A-1}$$

thus the strain is

$$\underline{\mathbf{s}}(r_1, r_2, t) = \begin{bmatrix} s_{11} & s_{12} \\ s_{12} & s_{22} \end{bmatrix} = \begin{bmatrix} -k\sin(kr_1 - \omega t) & 0 \\ 0 & 0 \end{bmatrix}. \tag{A-2}$$

Let's consider the case when we observe these strains from a rotated coordinate system (a fiber that sits at an angle $\theta$ from $(1, 0)$). By performing a tensor rotation we can write:

$$\begin{aligned} \underline{\mathbf{s}}(r_{1'}, r_{2'}, t) &= \begin{bmatrix} \cos(\theta) & \sin(\theta) \\ -\sin(\theta) & \cos(\theta) \end{bmatrix} \begin{bmatrix} -k\sin(kr_1 - \omega t) & 0 \\ 0 & 0 \end{bmatrix} \begin{bmatrix} \cos(\theta) & -\sin(\theta) \\ \sin(\theta) & \cos(\theta) \end{bmatrix} \\ &= \begin{bmatrix} -k\sin(kr_1 - \omega t)\cos^2(\theta) & k\sin(kr_1 - \omega t)\sin(\theta)\cos(\theta) \\ k\sin(kr_1 - \omega t)\sin(\theta)\cos(\theta) & -k\sin(kr_1 - \omega t)\sin^2(\theta) \end{bmatrix} \\ &= -k\sin(kr_1 - \omega t) \begin{bmatrix} \cos^2(\theta) & -\sin(\theta)\cos(\theta) \\ -\sin(\theta)\cos(\theta) & \sin^2(\theta) \end{bmatrix}, \end{aligned}$$

so the fiber would measure $s_{1'1'}$ which is $-k\sin(kr_1 - \omega t)\cos^2(\theta)$.

Now let's consider the case when we observe these strains from a coordinate system rotated $\pi/2$ from that one, plugging in $\cos(\theta + \pi/2) = -\sin(\theta)$ and $\sin(\theta + \pi/2) = \cos(\theta)$:

$$\begin{aligned} \underline{\mathbf{s}}(r_{1"}, r_{2"}, t) &= -k\sin(kr_1 - \omega t) \begin{bmatrix} \cos^2(\theta + \pi/2) & -\sin(\theta + \pi/2)\cos(\theta + \pi/2) \\ -\sin(\theta + \pi/2)\cos(\theta + \pi/2) & \sin^2(\theta + \pi/2) \end{bmatrix} \\ &= -k\sin(kr_1 - \omega t) \begin{bmatrix} \sin^2(\theta) & \cos(\theta)\sin(\theta) \\ \sin(\theta)\cos(\theta) & \cos^2(\theta) \end{bmatrix}, \end{aligned}$$

so the fiber would measure $s_{1"1"}$ which is $-k\sin(kr_1 - \omega t)\sin^2(\theta)$. That means any measurements on this fiber are the same as measurements on the orthogonal fiber by a factor of $\tan^2(\theta)$. Therefore, while we expect the polarity of waves observed by these two fibers to be the same (since $\tan^2(\theta) \geq 0$), the amplitude ratio between their observations depends on the direction of the propagating wave.

## 2D propagation in orthogonal direction to particle motion

This is relevant to Love waves or S-waves. We'll use a coordinate system $(r_1, r_2)$ where again $r_1$ is the direction of propagation, but now $r_2$ is the direction of particle motion. The expression for displacement at position $(r_1, r_2)$ and time $t$ of a monochromatic plane wave with frequency $\omega$ and wavenumber $k$ is

$$\mathbf{d}(r_1, r_2, t) = (0, \cos(kr_1 - \omega t)), \tag{A-3}$$

thus the strain is

$$\underline{\mathbf{s}}(r_1, r_2, t) = \begin{bmatrix} s_{11} & s_{12} \\ s_{12} & s_{22} \end{bmatrix} = \begin{bmatrix} 0 & \frac{-k}{2}\sin(kr_1 - \omega t) \\ \frac{-k}{2}\sin(kr_1 - \omega t) & 0 \end{bmatrix}. \tag{A-4}$$

Let's consider the case when we observe these strains from a rotated coordinate system (a fiber that sits at an angle $\theta$ from $(1, 0)$). By performing a tensor rotation we can write:

$$\begin{aligned}
\underline{\mathbf{s}}(r_{1'}, r_{2'}, t) &= \begin{bmatrix} \cos(\theta) & \sin(\theta) \\ -\sin(\theta) & \cos(\theta) \end{bmatrix} \begin{bmatrix} 0 & \frac{-k}{2}\sin(kr_1 - \omega t) \\ \frac{-k}{2}\sin(kr_1 - \omega t) & 0 \end{bmatrix} \begin{bmatrix} \cos(\theta) & -\sin(\theta) \\ \sin(\theta) & \cos(\theta) \end{bmatrix} \\
&= \begin{bmatrix} \sin(\theta)\frac{-k}{2}\sin(kr_1 - \omega t) & \cos(\theta)\frac{-k}{2}\sin(kr_1 - \omega t) \\ \cos(\theta)\frac{-k}{2}\sin(kr_1 - \omega t) & -\sin(\theta)\frac{-k}{2}\sin(kr_1 - \omega t) \end{bmatrix} \begin{bmatrix} \cos(\theta) & -\sin(\theta) \\ \sin(\theta) & \cos(\theta) \end{bmatrix} \\
&= -\frac{k}{2}\sin(kr_1 - \omega t) \begin{bmatrix} 2\sin(\theta)\cos(\theta) & \cos^2(\theta) - \sin^2(\theta) \\ \cos^2(\theta) - \sin^2(\theta) & 2\sin(\theta)\cos(\theta) \end{bmatrix}.
\end{aligned}$$

Hence, our fiber at angle $\theta$ would observe $s_{1'1'}$ of the rotated strain tensor which is $-k\sin(kr_1 - \omega t)\sin(\theta)\cos(\theta)$.

Now let's say we also wanted to observe the strains from a coordinate system that had been rotated $\pi/2$ from that one, we just have to plug in the identities $\cos(\theta + \frac{\pi}{2}) = -\sin(\theta)$ and $\sin(\theta + \frac{\pi}{2}) = \cos(\theta)$:

$$\begin{aligned}
\underline{\mathbf{s}}(r_{1"}, r_{2"}, t) &= \begin{bmatrix} \cos(\theta + \frac{\pi}{2}) & \sin(\theta + \frac{\pi}{2}) \\ -\sin(\theta + \frac{\pi}{2}) & \cos(\theta + \frac{\pi}{2}) \end{bmatrix} \begin{bmatrix} 0 & \frac{-k}{2}\sin(kr_1 - \omega t) \\ \frac{-k}{2}\sin(kr_1 - \omega t) & 0 \end{bmatrix} \cdots \\
&\quad \cdots \begin{bmatrix} \cos(\theta + \frac{\pi}{2}) & -\sin(\theta + \frac{\pi}{2}) \\ \sin(\theta + \frac{\pi}{2}) & \cos(\theta + \frac{\pi}{2}) \end{bmatrix} \\
&= -\frac{k}{2}\sin(kr_1 - \omega t) \begin{bmatrix} 2\sin(\theta + \frac{\pi}{2})\cos(\theta + \frac{\pi}{2}) & \cos^2(\theta + \frac{\pi}{2}) - \sin^2(\theta + \frac{\pi}{2}) \\ \cos^2(\theta + \frac{\pi}{2}) - \sin^2(\theta + \frac{\pi}{2}) & 2\sin(\theta + \frac{\pi}{2})\cos(\theta + \frac{\pi}{2}) \end{bmatrix} \\
&= -\frac{k}{2}\sin(kr_1 - \omega t) \begin{bmatrix} -2\cos(\theta)\sin(\theta) & \sin^2(\theta) - \cos^2(\theta) \\ \sin^2(\theta) - \cos^2(\theta) & -2\cos(\theta)\sin(\theta) \end{bmatrix}.
\end{aligned}$$

Therefore, our fiber at angle $\theta + \frac{\pi}{2}$ would observe $s_{1"1"}$ of the rotated strain tensor which is $k\sin(kr_1 - \omega t)\sin(\theta)\cos(\theta)$, which is exactly -1 times the observation of the fiber at angle $\theta$.

In conclusions, no matter what direction our wave is coming from relative to the fibers, the two fibers in perpendicular directions will always observe this type of plane wave with opposite signs (one sees compression while the other sees extension, and vice-versa).